ADVANCED ENERGY MATERIALS
www.advenergymat.de

Extremely Flexible Transparent Conducting Electrodes for Organic Devices

Sunghoon Jung, Sunghun Lee, Myungkwan Song, Do-Geun Kim, Dae Sung You, Jong-Kuk Kim, Chang Su Kim, Tae-Min Kim, Kwon-Hyeon Kim, Jang-Joo Kim and Jae-Wook Kang**

Extremely flexible transparent conducting electrodes are developed using a combination of metal-embedding architecture into plastic substrate and ultrathin transparent electrodes, which leads to highly transparent (optical transmittance ≈93% at a wavelength of 550 nm), highly conducting (sheet resistance ≈13 Ω □$^{-1}$), and extremely flexible (bending radius ≈ 200 μm) electrodes. The electrodes are used to fabricate flexible organic solar cells and organic light-emitting diodes that exhibit performance similar or superior to that of devices fabricated on glass substrates. Moreover, the flexible devices do not show degradation in their performance even after being folded with a radius of ≈200 μm.

1. Introduction

Flexible organic optoelectronic devices such as organic light-emitting diodes (OLEDs) and organic solar cells (OSCs) require transparent conducting electrodes (TCEs) that have high transparency and conductivity to be fabricated on plastic substrates. Indium tin oxide (ITO), the material most commonly used in the display industry, is not the most suitable for the fabrication of flexible devices because it is brittle and cracks easily under bending stress.[1,2] At present, several classes of flexible transparent electrodes, including those based on graphene,[1–4] metal nanowires,[5–9] conducting polymers,[10–13] and carbon nanotubes,[14–16] are being investigated. However, despite their strong potential as replacements for ITO these materials suffer from the classic trade-off between optical transmittance and electrical conductivity. Thicker layers afford higher conductivity, but this increase comes at the expense of optical transmittance and vice versa. In addition, large-area organic devices built using flexible transparent conducting electrodes based on these materials exhibit low efficiency, owing to the low conductivity of TCEs, in the absence of additional metal grids.[17–22]

It is possible to improve the conductivity of TCEs by incorporating metal grids in the organic devices. These metal grids are either deposited by thermal evaporation using a shadow mask,[17,18] patterned by lithographic methods,[19,20] or printed.[21,22] In organic devices, however, there is a limit to how thick the metal grids deposited beneath the organic layer can be. Because the organic layer is extremely thin (typically a few hundred nanometers in thickness), there is the possibility of there being electrical short-circuiting between the metal grids and the top electrode. To prevent this, researchers have tried inserting an insulating layer between the metal grids and the organic layers.[19] However, this process increases the manufacturing cost. Electrical short circuiting due to the use of printed metal grids can be prevented by embedding the grids in a polymer substrate.[24,25] Recently, a damascene process was used to fabricate a metal-embedding flexible substrate (MEFS). The process involved the fabrication of trench-like structures on flexible substrates using imprint lithography. Metal was deposited in the trench-like patterns and this was followed by the removal of any superfluous metal film by chemical-mechanical polishing.[23] However, this process is expensive.

Here we report a universal method to overcome this trade-off by using a combination of metal-embedding architecture into plastic substrate and ultrathin transparent electrodes, leading to highly transparent (optical transmittance ≈93% at a wavelength of 550 nm), highly conducting (sheet resistance ≈13 Ω □$^{-1}$) and extremely flexible (bending radius ≈200 μm) electrodes with very smooth surface. These electrodes were used to fabricate flexible organic devices that exhibited performances similar or superior to that of devices fabricated on glass substrate. In addition, these fabricated flexible devices did not show degradation in their performance even after being folded with a radius of ≈200 μm.

S. Jung, Dr. M. Song, Dr. D.-G. Kim, D. S. You, Dr. J.-K. Kim, Dr. C. S. Kim
Surface Technology Division
Korea Institute of Materials Science (KIMS)
Changwon, 641-831, Republic of Korea
S. Lee, T.-M. Kim, K.-H. Kim, Prof. J.-J. Kim
OLEDs Center
WCU Hybrid Materials Program
Department of Materials Science and Engineering
Seoul National University, Seoul, 151-744, Republic of Korea
E-mail: jjkim@snu.ac.kr
Prof. J.-W. Kang
Professional Graduate School of Flexible and Printable Electronics
Department of Flexible and Printable Electronics
Chonbuk National University
Jeonju, 561-756, Republic of Korea
E-mail: jwkang@jbnu.ac.kr

DOI: 10.1002/aenm.201300474

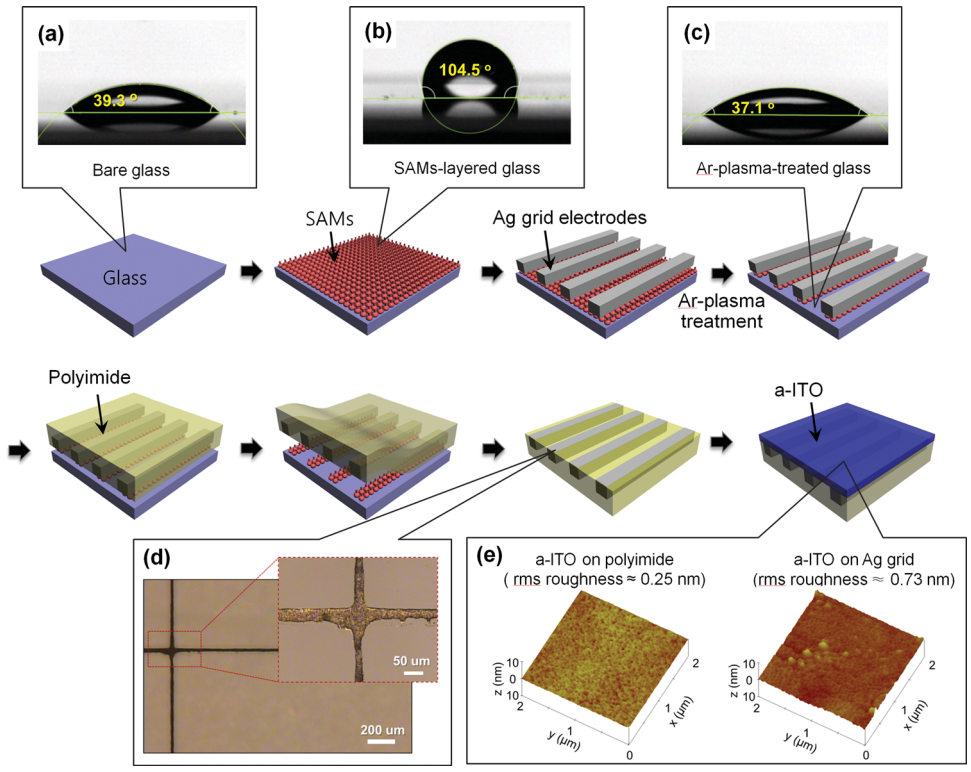

Figure 1. Schematic of the process for fabricating the TCEs on the MEFS. Photographs of the measured contact angle of a) bare glass, b) SAM-layered glass, and c) Ar-plasma-treated glass. d) Photographs of the Ag-grid-embedding flexible substrate. The printed Ag grid has a width of ≈39 ± 16 μm. e) AFM images of ≈20-nm-thick a-ITO films deposited on a polyimide film and a printed Ag grid electrode.

2. Results and Discussion

We have developed a new method for fabricating extremely flexible TCEs on MEFSs with very smooth surfaces without requiring chemical-mechanical polishing. The process for fabricating the TCEs on the MEFSs is explained schematically in **Figure 1**. The self-assembled monolayer (SAM) was formed on the glass substrate using 1H,1H,2H,2H-perfluorooctyltrichlorosilane, turning the surface of the substrate hydrophobic (change of contact angle from ≈39.3° to ≈104.5°). Ag grids, having a thickness of ≈1.3 μm and width of ≈39 μm, were printed using the gravure printing method on the SAM-layered glass substrate. Before the printing of the polymer solution to form the flexible substrates, the glass surfaces were subjected to a mild Ar plasma treatment to remove the SAM resulting in hydrophilic surfaces (contact angle of ≈37.1°). Subsequently, the polyimide (PI) solution was coated on top of the Ag grid printed on the glass substrate. This was followed by a thermal curing process to form a flexible substrate. Then the cured PI film, which had a thickness of ≈40 μm, was detached from the glass substrate, resulting in the Ag-grid-embedding flexible substrate, i.e., the MEFS. Finally, a 20-nm-thick layer of amorphous ITO (a-ITO) was deposited on the MEFS by a magnetron sputtering process to fabricate the TCE.

Cross-sectional scanning electron microscopy (SEM) images of a completed a-ITO-on-MEFS (a-ITO/MEFS) film are shown in **Figure 2**a. They show clearly that the printed Ag grid is well embedded within the PI substrate and that it has a flat top surface. It can also be seen that the a-ITO electrode is in direct contact with the metal grid, which had a very smooth surface (root mean square (rms) surface roughness of <1 nm and maximum peak-to-valley height of <10 nm, Figure 1e). A number of different grid patterns on the substrate 21 cm × 30 cm in size could be formed with ease using the process, as shown in Figure 2b.

Figure 3a plots the transmittance of the a-ITO/MEFS film at a wavelength of 550 nm ($T_{550\ nm}$) against its sheet resistance (R_{sheet}). The transmittances of other representative TCEs are included in the figure for comparison. Here, the ratio σ_{DC}/σ_{Op}, where σ_{DC} is the direct current conductivity and σ_{Op} is the optical conductivity of the a-ITO/MEFS film, can be regarded as a figure of merit (FoM) with its high values indicating that the TCE exhibited desirable properties.[7] The a-ITO/MEFS films exhibited FoM values ranging from 150 to 2500. These values of the FoM was comparable to those of c-ITO films (FoM ≈ 2000) and much higher than those recently reported for graphene[2] (FoM ≈ 120), and films based on Ag-nanowires[7,9] (FoM ≈ 40–400), poly(3,4-ethylenedioxythiophene):poly(styrene sulphonate) (PEDOT:PSS)[12] (FoM ≈ 40), and carbon nanotubes (CNTs)[15] (FoM ≈ 30).

Increasing the number of Ag grid electrodes per unit length (or area), i.e., reducing the spacing between the Ag grids, lowered the R_{sheet} of the a-ITO/MEFS film. It should be noted that the decrease in the optical transmittance of the a-ITO/MEFS

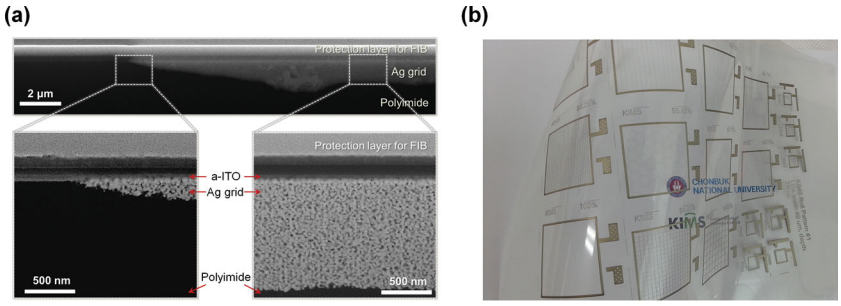

Figure 2. a) Cross-sectional SEM images of the a-ITO/MEFS film and b) photograph of a fabricated MEFS (21 cm × 30 cm).

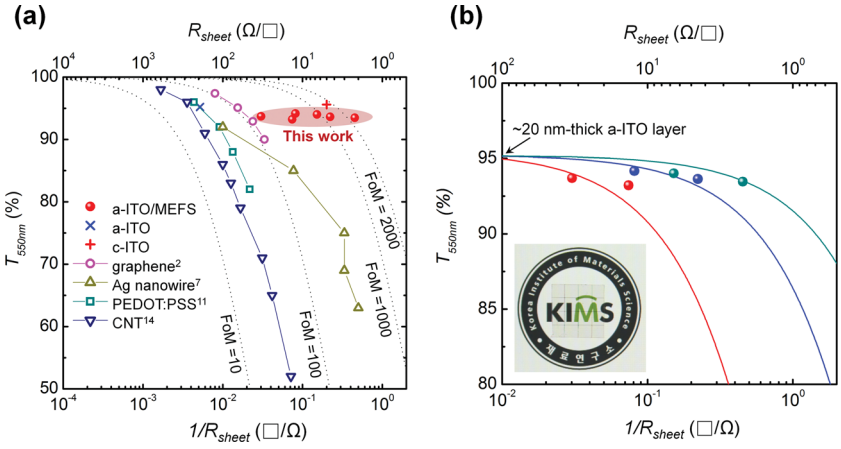

Figure 3. a) Transmittances of the a-ITO/MEFS films measured at 550 nm ($T_{550\ nm}$) plotted as a function of their sheet resistances (R_{sheet}). For comparison, the transmittances of c-ITO, graphene, Ag nanowire, PEDOT:PSS, CNT, and a-ITO TCEs are also shown. The values of the figure of merit (FoM) are also plotted. b) The $T_{550\ nm}$ value as a function of the R_{sheet} of a-ITO/MEFS films and the effect of the conductivities of the metal grids on the performance of the a-ITO/MEFS film. The data shown are for a printed Ag grid (red, $R_{sheet,\ Ag} \approx 0.25\ \Omega\ \square^{-1}$) and vacuum-deposited Cu grid (blue, $R_{sheet,\ cu} \approx 0.05\ \Omega\ \square^{-1}$; green, $Rs_{heet,\ cu} \approx 0.02\ \Omega\ \square^{-1}$). The inset shows a fabricated a-ITO/MEFS film having $R_{sheet} \approx 2\ \Omega\ \square^{-1}$ at $T_{550nm} \approx 93.5\%$.

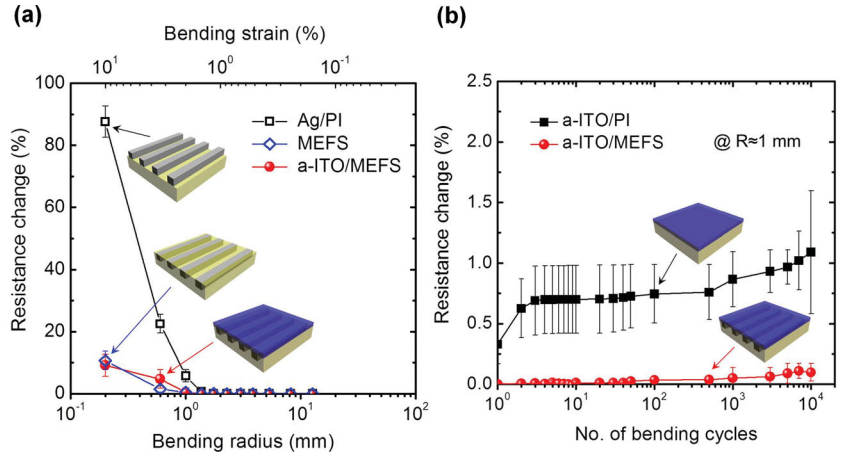

Figure 4. a) The measured changes in the resistances of Ag grids printed on a polyimide film (Ag/PI), an Ag-metal-embedding flexible substrate (MEFS), and a ≈20-nm-thick a-ITO/MEFS film as a function of the bending radius during compressive bending. b) Change in the resistance of a ≈20-nm-thick a-ITO-on-PI film (a-ITO/PI) and the ≈20-nm-thick a-ITO/MEFS film as a function of the number of bending cycles with the bending radius being ≈1 mm.

film with the reduced grid spacing was quite small. For example, as shown in Figure 3b, a 20-nm-thick a-ITO layer had an $R_{sheet} \approx 194\ \Omega\ \square^{-1}$ at $T_{550nm} \approx 95\%$. However, after being coated on the MEFS, the film exhibited a dramatic reduction in its R_{sheet} value to $\approx 13\ \Omega\ \square^{-1}$. This reduction was accompanied by a decrease of only ≈2% in the $T_{550\ nm}$ value of the film (see Supporting Information Figure 2). These experimentally obtained results (solid circles) matched very well with those theoretically predicted (solid line) on the basis of Ohm's law (see also Supporting Information Figure 1). The use of a vacuum-deposited metal grid can further reduce the R_{sheet} value while keeping the optical transmittance unchanged. For instance, when Cu grid electrodes patterned by lithographic method were used, the characteristics of the a-ITO/MEFS film improved significantly ($R_{sheet} \approx 7\ \Omega\ \square^{-1}$ at $T_{550nm} \approx 94\%$ and $R_{sheet} \approx 2\ \Omega\ \square^{-1}$ at $T_{550nm} \approx 93.5\%$), leading to the elimination of the trade-off between transmittance and conductivity (Figure 3b). These data clearly demonstrate that extremely smooth TCEs exhibiting both high conductivity and high transmittance at the same time can be obtained by overcoming the trade-off between transmittance and conductivity.

Another advantage of the MEFS is its durability under extreme mechanical bending. **Figure 4**a shows the post-bending changes in the resistances of the flexible TCE films as a function of the bending radius (R); the values shown are the averages of five samples. The bending induced compressive stresses in the films. The percentage change in the resistance of the flexible electrode can be expressed as $\Delta\Omega\Omega_0^{-1}$, where $\Delta\Omega$ is the actual change in the resistance after bending and Ω_0 is the initial resistance. In spite of the ITO films being brittle, the 20-nm-thick a-ITO/MEFS film showed high mechanical flexibility, with the percentage change in its resistance being small (≈10%). This was true even after it had been bent with a bending radius R of approximately 200 μm, which corresponded to a bending strain (ε) of ≈10%, with $\varepsilon = h_s/(2R)$, where h_s is the substrate thickness.[25] This percentage change in the resistance was much smaller than that for a 20-nm-thick a-ITO/PI film ($\Delta\Omega\Omega_0^{-1} \approx 930\%$) (Supporting Information Figure 3) and the printed Ag grid/PI film ($\Delta\Omega\Omega_0^{-1} \approx 87\%$). Moreover, the a-ITO/MEFS film showed excellent bending fatigue strength, as shown in Figure 4b, where the R was fixed at ≈1.0 mm, which corresponded to $\varepsilon \approx 2.0\%$. Even after being

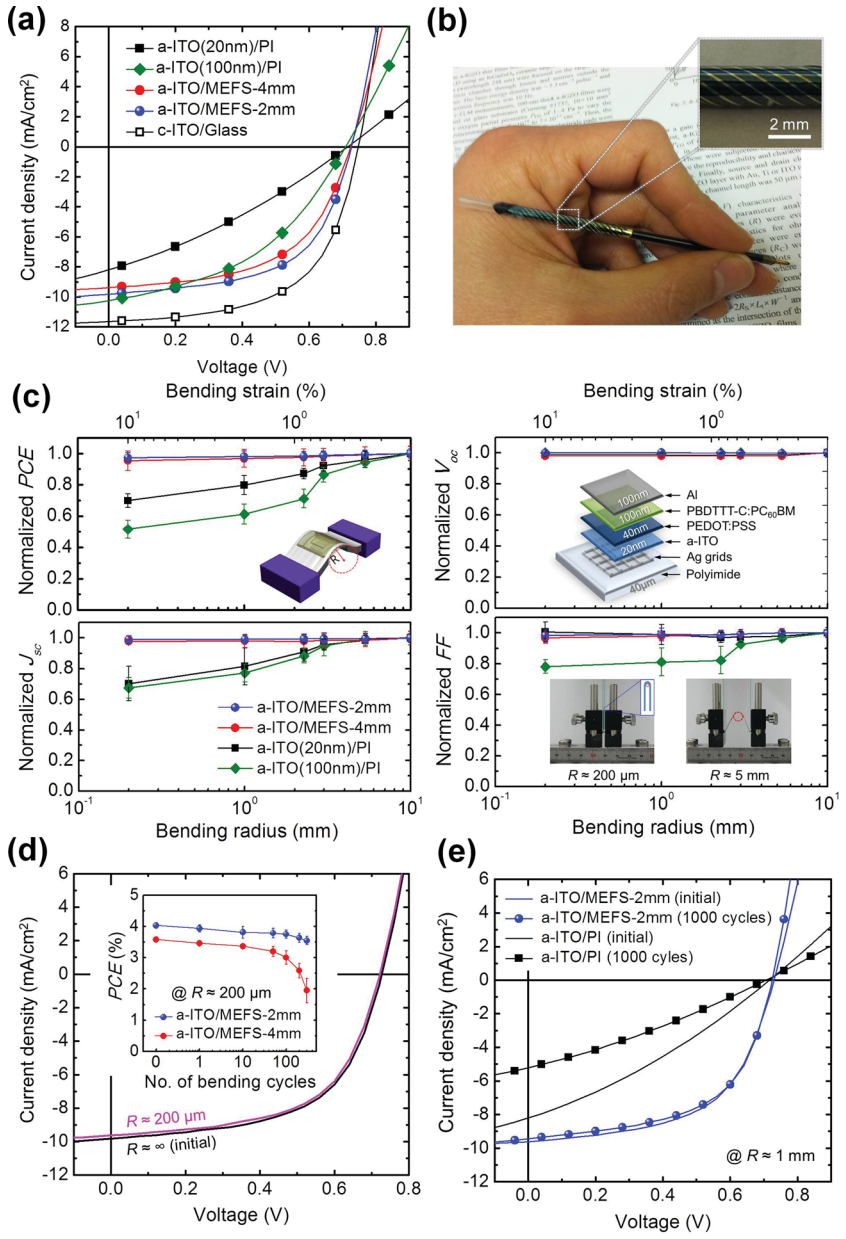

Figure 5. a) Current density–voltage characteristics of the OSCs fabricated using different TCEs. b) A photograph of a flexible OSC and a photograph of one such device wrapped around a cylinder with a radius of ≈1 mm. c) The measured PCE, V_{oc}, J_{sc}, and FF values of the flexible OSCs as a function of the bending radius during compressive bending, normalized to the initial value. The top inset shows a schematic of a flexible OSC and the bottom inset shows the bending process. d) The current density–voltage characteristics were measured in the flat state as well as while the OSCs were bent with a radius of ≈200 μm. The measured PCE values as a function of the folding cycles at a radius of ≈200 μm are shown in the inset. e) The current density–voltage characteristics of the OSCs after being bent a 1000 times with a bending radius of ≈1 mm.

bent 10 000 times, the a-ITO/MEFS film exhibited almost the same $\Delta\Omega\Omega_0^{-1}$ value (≈0.1%), whereas that of the a-ITO/PI film increased slightly (≈1%), when averaged over five samples.

We fabricated a series of flexible OSCs and green phosphorescent OLEDs using the a-ITO/MEFS films. A number of a-ITO/MEFS films with different metal grid configurations (2 mm spacing and 4 mm spacing; Supporting Information Figure 4) were used. These OSCs and OLEDs were compared with devices fabricated on a-ITO-coated PI substrates and c-ITO-coated glass substrates. **Figure 5**a shows the current density–voltage (*J*–*V*) characteristics of the OSCs fabricated using the a-ITO/MEFS films with various grid spacings, measured under simulated AM 1.5G illumination. In addition, the averages of the values of five samples are listed in **Table 1**. A blend of poly[(4,8-bis-(2-ethylhexyloxy)-benzo[1,2-b:4,5-b′] dithiophene)-2,6-diyl-alt-(4-(2-ethylhexanoyl)-thieno[3,4-b]thiophene)-2,6-diyl] (PBDTTT-C)[26,27] and [6,6]-phenyl-C_{61}-butyric acid methyl ester (PCBM) was used as the photoactive layer in the OSCs. The OSC fabricated using the a-ITO/MEFS film with the 2 mm grid spacing (a-ITO/MEFS-2mm) showed a power conversion efficiency (PCE) of ≈4.00% and a fill factor (FF) of ≈0.567. These values were higher than those of the a-ITO/MEFS-4mm device (PCE ≈ 3.65% and FF ≈ 0.543) and much higher than those of the devices fabricated using the 20-nm-thick a-ITO/PI film (PCE ≈ 1.80% and FF ≈ 0.307), 100-nm-thick a-ITO/PI film (PCE ≈ 3.33% and FF ≈ 0.449) and MEFS-2mm film (PCE ≈ 0.07% and FF ≈ 0.152) (Supporting Information Figure 5). As expected, the use of the finer grid resulted in higher PCE and FF values. This was due to the decrease in the R_{sheet} value.[18,28] A control device fabricated using the c-ITO/glass film showed a slightly higher PCE (≈4.69%) than that of the a-ITO/MEFS-2mm device. The primary reason for the slightly lower PCE value of the a-ITO/MEFS-2mm device was the decrease in its J_{sc} value, which resulted from the absorption of radiation of wavelengths smaller than ≈400 nm by the PI substrate. (Supporting Information Figure 6).

The MEFS-based OSCs were extremely flexible, as can be seen in Figure 5c,d. The a-ITO/MEFS devices did not show degradation in their parameters even when bent significantly (R ≈ 200 μm). In contrast, the a-ITO(20nm)/PI device showed a significant reduction in its PCE, which decreased to ≈70% of its initial value, and the device fabricated using a 100-nm-thick a-ITO/PI film exhibited an even more drastic reduction in its PCE, which decreased to ≈52% of its original value (Figure 5c and Supporting Information Figure 7). The a-ITO/MEFS devices also had excellent durability under repeated bending, exhibiting almost no change in its *J*–*V* characteristics even after 1000 bending cycles with R ≈ 1.0 mm. On the other hand, the a-ITO/PI devices displayed a significant

Table 1. Photovoltaic characteristics of the flexible OSCs under AM 1.5G illumination (100 mW cm^{-2}) after being bent at $R \approx 0.2$ mm and under 1000 bending cycles with $R \approx 1$ mm. The values are the averages of ≈5 samples of each device type and the error bars indicated the minimum and maximum values.

Device	Bending radius [mm]	No. of bending cycles	J_{sc} [mA cm^{-2}]	V_{oc} [V]	FF	PCE [%]
a-ITO(20nm)/PI	∞	0	8.050 ± 0.228	0.727 ± 0.020	0.307 ± 0.007	1.80 ± 0.06
	0.2	0	5.660 ± 0.909	0.718 ± 0.010	0.309 ± 0.020	1.25 ± 0.08
	1.0	1000	5.587 ± 0.691	0.711 ± 0.006	0.279 ± 0.029	1.10 ± 0.09
a-ITO(100nm)/PI	∞	0	10.293 ± 0.430	0.721 ± 0.022	0.449 ± 0.023	3.33 ± 0.16
	0.2	0	6.948 ± 0.695	0.706 ± 0.008	0.351 ± 0.020	1.72 ± 0.18
	1.0	1000	5.190 ± 0.499	0.712 ± 0.010	0.322 ± 0.021	1.18 ± 0.07
a-ITO/MEFS-4mm	∞	0	9.326 ± 0.417	0.721 ± 0.012	0.543 ± 0.014	3.65 ± 0.16
	0.2	0	9.128 ± 0.322	0.722 ± 0.009	0.527 ± 0.019	3.47 ± 0.22
	1.0	1000	9.229 ± 0.452	0.721 ± 0.006	0.530 ± 0.017	3.52 ± 0.12
a-ITO/MEFS-2mm	∞	0	9.733 ± 0.260	0.726 ± 0.005	0.567 ± 0.010	4.01 ± 0.11
	0.2	0	9.633 ± 0.242	0.726 ± 0.006	0.558 ± 0.021	3.90 ± 0.12
	1.0	1000	9.575 ± 0.203	0.726 ± 0.002	0.561 ± 0.006	3.90 ± 0.05
c-ITO/glass	–	–	11.78 ± 0.120	0.740 ± 0.005	0.534 ± 0.010	4.69 ± 0.20

decrease in their PCE value (to ≈61% and ≈35% of the initial value for 20-nm-thick and 100-nm-thick ITO films, respectively) after being subjected to the same number of bending cycles (Figure 5e and Supporting InformationFigure 8). Moreover, the a-ITO/MEFS-2mm device showed excellent folding durability and exhibited only a small decrease in its PCE after 300 folding cycles (Figure 5d and Supporting Information Figure 9). The effect of the grids on device performance was more pronounced in case of the large-area OSCs as a shown in **Figure 6**. The PCE of the large-area flexible OSCs (with a cell area of ≈10.9 cm^2) increased dramatically, from ≈0.12% to ≈2.55%, with the use of a grid with a spacing of 0.7 mm. This, in turn, resulted in an increase in the FF (from ≈0.25 to ≈0.43), which showed that the performance of the a-ITO/MEFS devices was higher than that of the large-area c-ITO/glass devices (PCE ≈ 2.0% and FF ≈ 0.30) (Supporting Information Figure 10).

The performance of OLEDs is highly dependent on the surface roughness of the substrates used for the devices. Therefore, rough metal grid and TCE surfaces can lead to an increase in the leakage current in the devices, resulting in the failure of the OLEDs. We were able to fabricate extremely flexible and high-performance OLEDs using the a-ITO/MEFS films because of the extremely low surface roughness of the a-ITO-based TCE. The devices had the following structure: MEFS/a-ITO/MoO_3 (1 nm)/CBP (220 nm)/CBP:Ir(ppy)$_2$(acac) (15 nm)/TPBi (10 nm)/B3PYMPM (55 nm)/LiF/Al, where CBP is

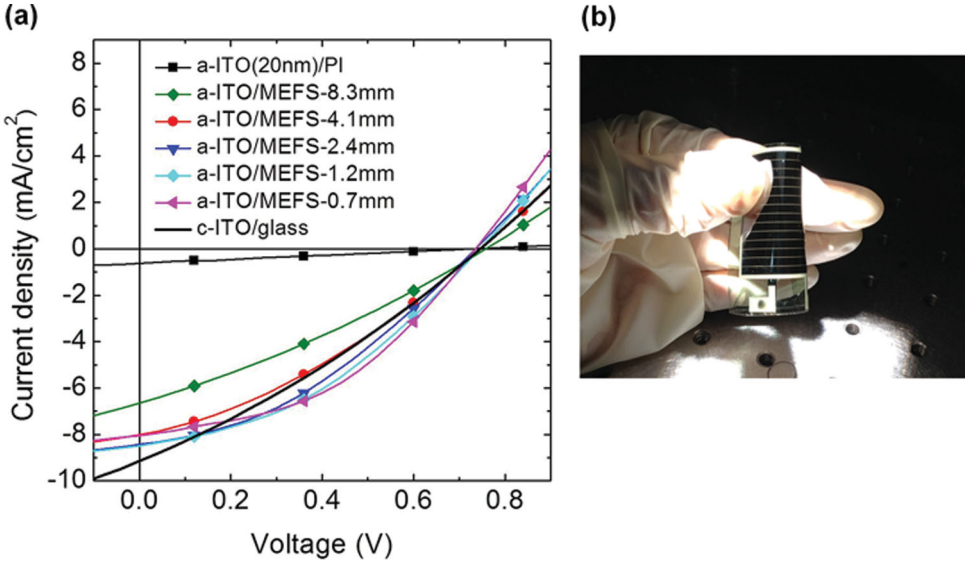

Figure 6. a) The current density-voltage characteristics of large-area (cell area of ≈10.9 cm^2) OSCs having different metal grid spacings and b) photograph of a large-area flexible OSC fabricated using a ≈20-nm-thick a-ITO-on-MEFS film with 2.4 mm grid spacing.

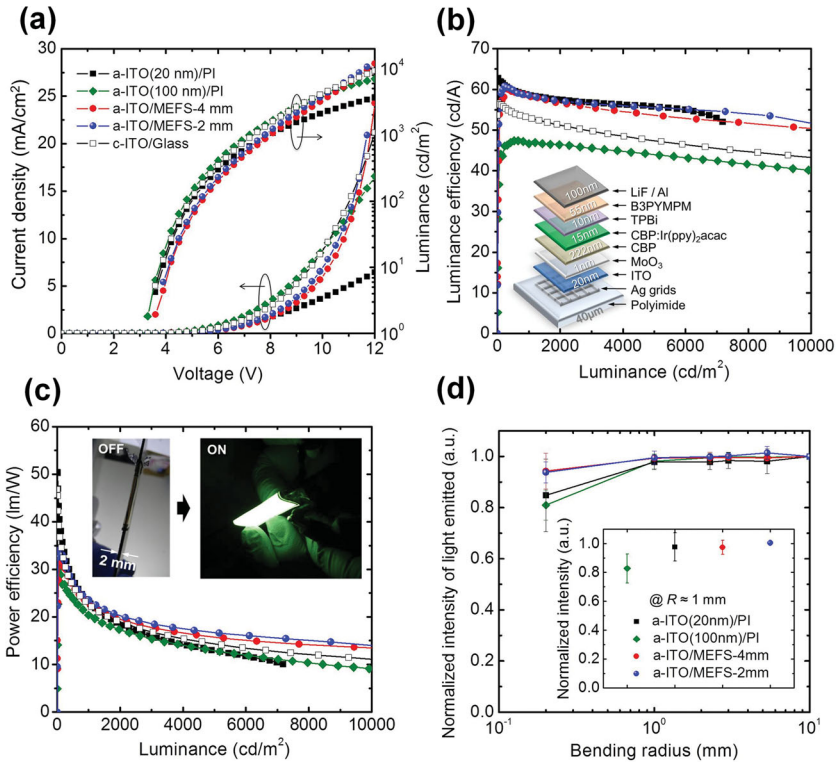

Figure 7. a) Current density-voltage characteristics of the OLEDs fabricated using different TCEs. b) Current efficiency-luminance characteristics of the OLEDs. The inset shows a schematic of the flexible OLEDs. c) Power efficiency-luminance characteristics of the OLEDs. The inset shows photographs of the large-area bendable OLEDs (5 cm × 5 cm). d) Measured intensity of the light emitted by the flexible OLEDs as a function of the bending radius during compressive bending, normalized to the initial value. The intensities of the light emitted measured after the bending of the OLEDs 1000 times with a bending radius of ≈1 mm are shown in the inset.

4′-*N*,*N*′-dicarbazole-biphenyl, $Ir(ppy)_2(acac)$ is bis(2-phenylpyridine)(acetylacetonate)iridium(III), TPBi is 2,2′,2″-(1,3,5-benzenetriyl)tris-[1-phenyl-1H-benzimidazole], and B3PYMPM is bis-4,6-(3,5-di-3-pyridylphenyl)-2-methylpyrimidine. The characteristic properties of these devices are shown in **Figure 7** and summarized in **Table 2**, and are compared with those of a control device fabricated on c-ITO-coated glass substrate (Figure 7a–c). The luminance efficiency (LE) and power efficiency (PE) of the devices are shown in Figure 7b,c as a function of the luminance. The a-ITO/MEFS-2mm device showed a maximum LE of ≈59 cd A^{-1}, which was higher than that of the a-ITO(100nm)/PI (LE ≈ 48 cd A^{-1}) and c-ITO/glass (LE ≈ 54 cd A^{-1}) devices. Moreover, the LE of the a-ITO/MEFS-2mm device in the normal direction was maintained over 90% of the maximum value up to the luminance of 10,000 cd m^{-2}, resulting in a very small roll-off in the LE value (LE ≈ 53 cd A^{-1} at 10 000 cd m^{-2}, Table 2). In contrast, the c-ITO/glass device exhibited an LE of ≈42 cd A^{-1} at 10 000 cd m^{-2}, which corresponded to a roll-off of ≈22%. The a-ITO/MEFS devices also showed excellent mechanical flexibility, as can be seen in Figure 7d, with the decrease in the intensity of light emitted being small. The level of luminescence remained at ≈94% of the pretest value even after the device was bent with a bending radius of ≈200 μm. In contrast, the a-ITO/PI devices displayed a significant decrease in the intensity of the light emitted by them (to ≈85% and ≈81% of the initial value for 20-nm-thick and 100-nm-thick ITO films, respectively). The a-ITO/MEFS devices also had excellent durability under repeated bending, exhibiting almost no change in their emitting intensity even after 1000 bending cycles with $R \approx 1.0$ mm, whereas the 100-nm-thick a-ITO/PI device showed a significant decrease in its light intensity (≈83% of the initial value). A foldable large-area OLED, shown in Figure 7c, was also fabricated, with the emitting area being ≈10.9 cm^2 (several movies of the foldable OLEDs are available as Supporting Information Movies 1 and 2). These results demonstrate that the MEFS combined with the a-ITO electrode can be used to fabricate large-area flexible OSCs and solid-state lighting devices in the future. Furthermore, because ITO as a material is already being used in mass production and its electronic properties, including its work function, can be manipulated,[29,30] it should be possible to fabricate these new a-ITO-based electrodes, which help establish good electrical contact at the ITO/organic junction, using existing technology without any modification.

Table 2. The summary of flexible OLEDs performance. The values are the averages of ≈5 samples of each device type and the error bars indicated the minimum and maximum values.

Device	Maximum LE[a] [cd A^{-1}]	Maximum PE[b] [lm W^{-1}]	@1000 cd m^{-2}		@5000 cd m^{-2}		@10 000 cd m^{-2}	
			LE [cd A^{-1}]	PE [lm W^{-1}]	LE [cd A^{-1}]	PE [lm W^{-1}]	LE [cd A^{-1}]	PE [lm W^{-1}]
a-ITO(20nm)/PI	58.3 ± 4.4	43.4 ± 7.0	55.3 ± 3.3	20.7 ± 2.4	51.0 ± 4.7	11.2 ± 1.7	–	–
a-ITO(100nm)/PI	47.6 ± 4.6	31.1 ± 5.7	45.2 ± 4.1	19.6 ± 2.0	41.6 ± 2.9	12.1 ± 1.1	36.8 ± 3.2	8.1 ± 1.0
a-ITO/MEFS-4mm	59.0 ± 2.9	38.1 ± 7.8	57.0 ± 4.6	22.1 ± 2.5	52.3 ± 3.0	15.2 ± 1.1	49.4 ± 1.4	13.1 ± 0.9
a-ITO/MEFS-2mm	58.8 ± 4.0	33.2 ± 11.2	56.8 ± 5.3	22.8 ± 2.2	55.1 ± 1.7	16.5 ± 0.8	52.6 ± 2.7	14.3 ± 1.3
c-ITO/glass	54.3 ± 2.1	46.4 ± 0.6	51.8 ± 1.4	21.9 ± 0.8	46.1 ± 1.6	13.7 ± 0.6	42.3 ± 1.4	10.8 ± 0.5

[a]Maximum LE: maximum luminance efficiency; [b]Maximum PE: maximum power efficiency

3. Conclusion

In conclusion, we were able to fabricate extremely flexible organic devices using metal-embedded flexible substrate. The use of the metal grid and the ITO layer in combination resulted in an increase in conductivity without a reduction in the transmission and helped in overcoming the trade-off between them. By using this approach, the mass production of organic devices using direct printing processes, which are compatible with roll-to-roll manufacturing, should be possible. In addition, this approach could theoretically be applied to fabricate TCEs from different materials such as graphene, metal nanowires, carbon nanotubes, and conducting polymers as well. In other words, this approach could be a "universal" technique for fabricating flexible substrates.

4. Experimental Section

Fabrication of the MEFS: The glass substrates were cleaned with aceqtone and isopropyl alcohol (IPA) in preparation for the printing. The SAM was formed on the glass substrate using 1H, 1H, 2H, 2H-perfluorooctyltrichlorosilane (FOTS), causing the surface of the substrate to become hydrophilic. The Ag grids, which had a thickness of ≈1.3 μm and width of ≈39 μm, were fabricated on the SAM-layered glass substrates using a Ag paste (85% Ag content, Advanced Nano Product Co.,) and a gravure offset printing system (Roll Printer, DCN Co., Ltd.). The printed Ag grids were sintered by annealing at 200 °C for 1 h in a convection oven. This resulted in the resistivity of the grids being ≈3.0×10^{-5}Ω cm. The resistivity was measured by the four-point-probe method (MCP-T600, Mitsubishi Chemical Corporation) using a printed Ag thick film with dimensions of 2 cm × 2 cm. Before the printing of the polymer solution to form the flexible substrates, the glass surfaces were subjected to a mild Ar plasma treatment to remove the SAM. This turned the hydrophobic surfaces hydrophilic. The Ar plasma treatment was carried out for 1 min using a gas flow rate of 100 sccm, radio-frequency (RF) power of 150 W at 13.56 MHz, and working pressure of 2.0×10^{-4} atm. Subsequently, the polyimide (PI) solution (VTEC-PI-051, Richard Blaine International Inc.) was doctor-bladed on top of the Ag grid printed on the glass substrate. The polyimide solution was uniformly coated over the entire glass substrate (the substrate 21 cm × 30 cm in size), resulting in a layer of thickness of 400 μm, which formed a 40-μm-thick film after being thermally cured in an oven at 80 °C for 10 min and then at 200 °C for 10 min. After the curing process, the film was detached from the glass substrate, resulting in the Ag-grid-embedding flexible substrate, i.e., the MEFS. For the Cu-grid-embedding flexible substrate, the 0.68-μm-thick Cu ($R_{sheet,cu} \approx 0.05$ Ω □$^{-1}$) and 1.7-μm-thick Cu ($R_{sheet,cu} \approx 0.02$ Ω □$^{-1}$) films were deposited on a cleaned Si wafer substrate. After the Cu film was patterned via lithography using a photomask fabricated by printing Ag grids on glass, the PI solution was coated on top of the Cu grid patterned on the Si wafer substrate. After the thermal curing, the MEFS was detached from the Si wafer substrate.

The ITO film was deposited on top of the MEFS by RF-superimposed direct current (DC) magnetron sputtering while maintaining vacuum-like condition. An ITO target containing 10 wt% tin was used for the sputtering. The sputtering was performed at a base pressure of $<2.6 \times 10^{-9}$ atm and working pressure of ≈1.3×10^{-6} atm and the injection gas flow rate was 30 sccm for Ar and 0.3 sccm for O_2. The DC power was controlled by keeping the current constant (0.60 A), and 50 W of RF power was imposed on it simultaneously. The growth rate of the ITO film was 0.317 nm s^{-1}, and a film with a total thickness of ≈20 nm was deposited. The transmittances of the a-ITO/MEFS films were measured using an ultraviolet-visible (UV-vis) spectrophotometer (Cary 5000, Varian). The two-point-probe method was used to determine the sheet resistance of the a-ITO/MEFS films (Supporting Information Figure 11).

Fabrication of the Flexible OSCs and OLEDs: Prior to the spin coating of the organic layers, the a-ITO/MEFS film was subjected to an ultraviolet (UV)/ozone treatment for 90 s. For the flexible OSCs, a buffer layer of poly(3,4-ethylenedioxylenethiophene) (PEDOT-PSS) (Clevios P) diluted with isopropyl alcohol (IPA) in the ratio PEDOT-PSS:IPA = 1:2 was prepared using a spin coater. The coated layer was passed through a 0.45 μm filter, which resulted in the final thickness of the layer being ≈40 nm. The PEDOT-PSS-coated substrate was dried at 120 °C for 5 min on a hot plate in a glove box. A blend of PBDTTT-C (1-material) and PCBM (Nano-C) in a 1:2 mass ratio was prepared in 1,2-dichlorobenzene with the total concentration being 30 mg/ml. The solution was stirred for more than 12 h at 50 °C in a nitrogen atmosphere. A PBDTTT-C:PCBM film, which acted as the photoactive layer, was then spin cast on the substrate at 800 rpm over a period of 40 s. The thickness of this film was ≈100 nm. Finally, a 100-nm-thick Al electrode was deposited on the PEDOT:PSS layer by thermal evaporation at 3.9×10^{-9} atm with a deposition rate of ≈6 Å/s. The cell area of the OSCs was ≈0.64 cm^2. A control device was also fabricated using the ≈300-nm-thick c-ITO/glass film ($T_{550nm} \approx 95\%$ and $R_{sheet} \approx 5$ Ω □$^{-1}$) with same cell area.[9]

For the flexible OLEDs, prior to the deposition of the organic layers, the a-ITO/MEFS film was cleaned with ultrapurified water, acetone, and isopropyl alcohol and then dried in an oven at 80 °C. It was then subjected to an UV/ozone treatment for 90 s. The structure of the OLEDs was the following: substrate/TCE/MoO_3 (1 nm)/CBP (220 nm)/CBP:Ir(ppy)$_2$(acac) (8 wt%, 15 nm)/TPBi (10 nm)/B3PYMPM (55 nm)/LiF (1 nm)/aluminium (100 nm), where CBP is 4′-*N*,*N*′-dicarbazole-biphenyl, Ir(ppy)$_2$(acac) is bis(2-phenylpyridine)(acetylacetonate)iridium(III), TPBi is 2,2′,2″-(1,3,5-benzenetriyl)tris-[1-phenyl-1H-benzimidazole], and B3PYMPM is bis-4,6-(3,5-di-3-pyridylphenyl)-2-methylpyrimidine. All the OLEDs were fabricated under a base pressure of $<6.5 \times 10^{-10}$ atm. The control device fabricated using the ≈100-nm thick c-ITO/glass ($T_{550nm} \approx 93\%$ and $R_{sheet} \approx 20$ Ω □$^{-1}$) with the emitting area of ≈0.64 cm^2.

Measurements of the Flexible Devices: The *J*–*V* characteristics of the OSCs were measured under simulated AM 1.5 illumination having an intensity of 100 mW cm^{-2} (Pecell Technologies Inc., PEC-L11). The intensity of the sunlight-simulating illumination was calibrated using a standard Si photodiode detector with a KG-5 filter. The *J*–*V* curves were recorded automatically using a Keithley 2410 source measurement unit by illuminating the OSC prepared. The quantum efficiency measurement system (Oriel IQE-200) used to determine the incident-photon-to-charge-carrier efficiency (IPCE) comprised a 250 W quartz-tungsten-halogen (QTH) lamp as the light source, a monochromator, an optical chopper, a lock-in amplifier, and a calibrated silicon photodetector. The performances of all the OLEDs were measured in air immediately after they had been removed from the nitrogen-containing glove box. The current density-voltage-luminance (*J*–*V*–*L*) characteristics of the devices were measured using a Keithley 237 semiconductor parameter analyzer and a spectrophotometer (PR-650, Photo Research, Inc.).

Supporting Information

Supporting Information is available from the Wiley Online Library or from the author.

Acknowledgements

S.J., S.L., and M.S. contributed equally to this work. This study was supported by the New and Renewable Energy Program of the Korea Institute of Energy Technology Evaluation and Planning (KETEP) (Grant Nos. 20113010010030), funded by the Ministry of the Knowledge Economy, Republic of Korea.

Received: May 3, 2013
Revised: June 18, 2013
Published online: July 23, 2013

[1] T.-H. Han, Y. Lee, M.-R. Choi, S.-H. Woo, S.-H. Bae, B. H. Hong, J.-H. Ahn, T.-W. Lee, *Nat. Photonics* **2012**, *6*, 105.
[2] S. Bae, H. Kim, Y. Lee, X. Xu, J.-S. Park, Y. Zheng, J. Balakrishnan, T. Lei, H. R. Kim, Y. I. Song, Y.-J. Kim, K. S. Kim, B. Ozyilmaz, J.-H. Ahn, B. H. Hong, S. Iijima, *Nat. Nanotechnol.* **2010**, *5*, 574.
[3] F. Bonaccorso, Z. Sun, T. Hasan, A. C. Ferrari, *Nat. Photonics* **2010**, *4*, 611.
[4] G. Eda, G. Fanchini, M. Chhowalla, *Nat. Nanotechnol.* **2008**, *3*, 270.
[5] J.-Y. Lee, S. T. Connor, Y. Cui, P. Peumans, *Nano Lett.* **2008**, *8*, 689.
[6] J. Krantz, M. Richter, S. Spallek, E. Spiecker, C. J. Brabec, *Adv. Funct. Mater.* **2011**, *21*, 4784.
[7] S. De, T. M. Higgins, P. E. Lyons, E. M. Doherty, P. N. Nirmalraj, W. J. Blau, J. J. Boland, J. N. Coleman, *ACS Nano* **2009**, *3*, 1767.
[8] D.-S. Leem, A. Edwards, M. Faist, J. Nelson, D. D. C. Bradley, J. C. de Mello, *Adv. Mater.* **2011**, *23*, 4371.
[9] M. Song, D. S. You, K. Lim, S. Park, S. Jung, C. S. Kim, D.-H. Kim, D.-G. Kim, J.-K. Kim, J. Park, Y.-C. Kang, J. Heo, S.-H. Jin, J. H. Park, J.-W. Kang, *Adv. Funct. Mater.* DOI: 10.1002/adfm.201202646.
[10] S.-I. Na, S.-S. Kim, J. Jo, D.-Y. Kim, *Adv. Mater.* **2008**, *20*, 4061.
[11] M. Kaltenbrunner, M. S. White, E. D. Glowacki, T. Sekitani, T. Someya, N. S. Sariciftici, S. Bauer, *Nat. Commun.* **2012**, *3*, 770.
[12] Y. H. Kim, C. Sachse, M. L. Machala, C. May, L. Muller-Meskamp, K. Leo, *Adv. Funct. Mater.* **2011**, *21*, 1076.
[13] K. Lee, S. Cho, S. H. Park, A. J. Heeger, C.-W. Lee, S.-H. Lee, *Nature* **2006**, *441*, 65.
[14] Z. Wu, Z. Chen, X. Du, J. M. Logan, J. Sippel, M. Nikolou, K. Kamaras, J. R. Reynolds, D. B. Tanner, A. F. Hebard, A. G. Rinzler, *Science* **2004**, *305*, 1273.
[15] H.-Z. Geng, K. K. Kim, K. P. So, Y. S. Lee, Y. Chang, Y. H. Lee, *J. Am. Chem. Soc.* **2007**, *129*, 7758.
[16] J. Li, L. Hu, L. Wang, Y. Zhou, G. Gruner, T. J. Marks, *Nano Lett.* **2006**, *6*, 2472.
[17] S.-Y. Park, Y.-J. Kang, S. Lee, D.-G. Kim, J.-K. Kim, J. H. Kim, J.-W. Kang, *Sol. Energy Mater. Sol. Cells* **2011**, *95*, 852.
[18] W. -I. Jeong, J. Lee, S.-Y. Park, J.-W. Kang, J.-J. Kim, *Adv. Funct. Mater.* **2011**, *21*, 343.
[19] S. Choi, W. J. Potscavage, Jr., B. Kippelen, *J. Appl. Phys.* **2009**, *106*, 054507.
[20] J. Zou, H.-L. Yip, S. K. Hau, A. K.-Y. Jen, *Appl. Phys. Lett.* **2010**, *96*, 203301.
[21] Y. Galagan, B. Zimmermann, E. W. C. Coenen, M. Jorgensen, D. M. Tanenbaum, F. C. Krebs, H. Gorter, S. Sabik, L. H. Slooff, S. C. Veenstra, J. M. Kroon, R. Andriessen, *Adv. Energy Mater.* **2012**, *2*, 103.
[22] F. C. Krebs, R. S ndergaard, M. J rgensen, *Sol. Energy Mater. Sol. Cells* **2011**, *95*, 1348.
[23] Y. Matsumura, Y. Enomoto, T. Tsuruoka, K. Akamatsu, H. Nawafune, *Langmuir* **2010**, *26*, 12448.
[24] P. Kuang, J.-M. Park, W. Leung, R. C. Mahadevapuram, K. S. Nalwa, T.-G. Kim, S. Chaudhary, K.-M. Ho, K. Constant, *Adv. Mater.* **2011**, *23*, 2469.
[25] S.-I. Park, J.-H. Ahn, X. Feng, S. Wang, Y. Huang, J. A. Rogers, *Adv. Funct. Mater.* **2008**, *18*, 2673.
[26] H.-Y. Chen, J. Hou, S. Zhang, Y. Liang, G. Yang, Y. Yang, L. Yu, Y. Wu, G. Li, *Nat. Photonics* **2009**, *3*, 649.
[27] M. Song, J.-W. Kang, D.-H. Kim, J.-D. Kwon, S.-G. Park, S. Nam, S. Jo, S. Y. Ryu, C. S. Kim, *Appl. Phys. Lett.* **2013**, *102*, 143303.
[28] J.-W. Kang, S.-P. Kim, D.-G. Kim, S. Lee, G.-H. Lee, J.-K. Kim, S.-Y. Park, J. H. Kim, H.-K. Kim, Y.-S. Jeong, *Electrochem. Solid-State Lett.* **2009**, *12*, H64.
[29] Y. Zhou, C. Fuentes-Hernandez, J. Shim, J. Meyer, A. J. Giordano, H. Li, P. Winget, T. Papadopoulos, H. Cheun, J. Kim, M. Fenoll, A. Dindar, W. Haske, E. Najafabadi, T. M. Khan, H. Sojoudi, S. Barlow, S. Graham, J.-L. Bredas, S. R. Marder, A. Kahn, B. Kippelen, *Science* **2012**, *336*, 327.
[30] M. G. Helander, Z. B. Wang, J. Qiu, M. T. Greiner, D. P. Puzzo, Z. W. Liu, Z. H. Lu, *Science* **2011**, *332*, 944.